Electron dynamics for high-intensity hollow electron beams

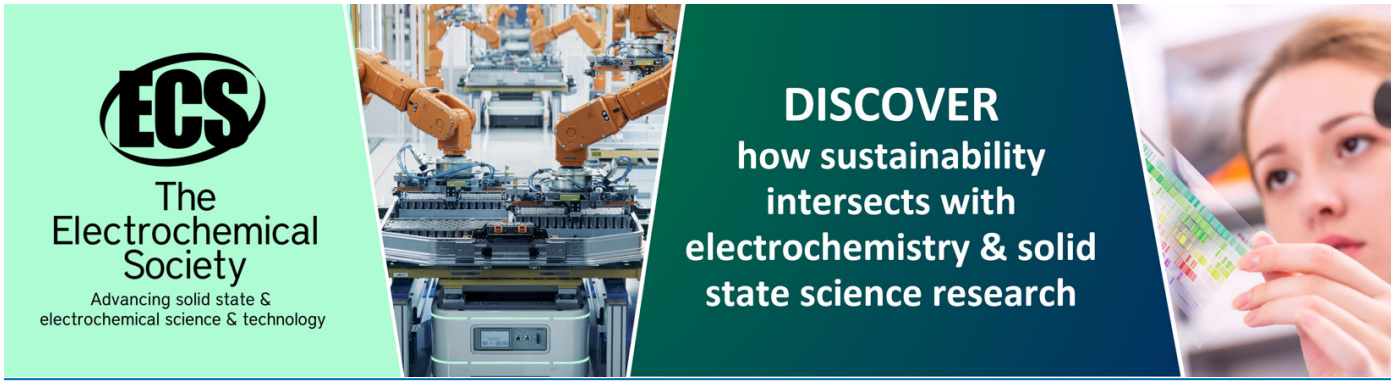

Published by IOP Publishing for Sissa Medialab

Received: *March 8, 2021*
Accepted: *March 10, 2021*
Published: *March 31, 2021*

ICFA Beam Dynamics Newsletter#81 —
Electron Lenses for Modern and Future Accelerators

Electron dynamics for high-intensity hollow electron beams

A. Rossi,[a,*] **D. Nikiforov,**[b] **M. Arsentyeva,**[b] **A. Barnyakov**[b] **and A. Levichev**[b]

[a] *European Organization for Nuclear Research,*
Esplanade des Particules 1, Meyrin, Geneva, Switzerland
[b] *Budker Institute of Nuclear Physics,*
11, Acad. Lavrentieva Pr., Novosibirsk, 630090 Russian Federation

E-mail: adriana.rossi@cern.ch

Abstract: Hollow Electron Lenses (HEL) will be installed at the High Luminosity Large Hadron Collider to provide a continuous and controlled depletion of beam halo particles by interaction with a superimposed hollow electron beam, of intensity as high as 5 A, and radii 1.1–2.2 mm for 7 TeV LHC operations. In this paper, issues related to the propagation of high intensity hollow electron beams are discussed and the simulations of the electron beam dynamics with feedback to the HEL design are presented. The main results are the rise of the electron beam accelerating voltage from 10 kV, as in the initial proposal, to 15 kV and the validation of the 5 T magnetic field at the main solenoids as being sufficient to guarantee a stable electron beam.

Keywords: Accelerator Applications; Accelerator modelling and simulations (multi-particle dynamics; single-particle dynamics)

*Corresponding author.

https://doi.org/10.1088/1748-0221/16/03/P03043

2021 JINST 16 P03043

Contents

2021 JINST 16 P03043

1 Introduction

The upgrade of the Large Hadron Collider to the High Luminosity (HL-LHC) project requires a way to control the level of the highly populated hadron beam halo and mitigate possible damage deriving from sudden movements of the beam orbit due to accident or failure [1]. Hollow Electron Lenses (HEL) have been designed to this purpose [1, 2] and provide a continuous and controlled depletion with a superimposed hollow electron beam. This method of collimation offers several advantages, since the electron beam does not introduce additional impedance, cannot be damaged by the hadron beam, its size and its intensity can be adjusted, and the depletion rate controlled by introducing non-linear dynamics [3, 4]. In order for the hadron beam core not to be affected by the HEL operation, the electrons must generate a hollow, axially symmetric electromagnetic field affecting only halo particles, ideally with zero field in the centre. This requires an electron beam with perfectly annular cross section, and evenly distributed electron density. After a brief introduction to the HL-LHC HEL, and its main parameters, in section 2, this paper reviews in section 3 the physics behind the dynamics of a high-intensity hollow electron beam, and introduces a quantitative way to theoretically evaluate the time of growth of diocotron instabilities, in section 3.2. Some results from numerical simulations are presented and discussed in section 4.

2 High Luminosity Hollow Electron Lens (HEL) parameters and requirements

The HEL was proposed [2] for LHC after successful experimental tests performed at FNAL [5–8], where both halo depletion and core preservation were demonstrated. The HEL is targeted at enabling active control of beam tails above 3 to 4 beam σ_h, with tail depletion efficiencies of the order of 90% over times of tens of seconds to minutes [1, 9]. At LHC, a suitable location for the HEL was found in the Interaction Region 4, between the two separation dipole magnets D3, where the LHC circulating beams are furthest apart, with an intra-beam distance of 420 mm. This space is required to lodge the super-conductive solenoid magnets necessary to confine and transport the electron beam. This region had, in addition, longitudinal available space, cryogenic services at proximity, low radiation environment, and space in the service adjacent tunnels [10]. Moreover, at the selected location, the LHC optics has been set for HEL operations, with quasi round and relatively large hadron beams (at the HEL nominal positions, $\beta_{(x,y)} = 280$ m, corresponding to a hadron beam $\sigma_h \approx 0.31$ mm [11]). This is an advantage since the electron beam should overlap with the hadron beam between 3.6 and 7.2 σ_h [1], corresponding to internal and external radii respectively of 1.1 mm and 2.2 mm, and squeezing the few Amperes electron beam in a cross section below the 1 mm size would make the beam more prone to instability, as discussed in the following. Furthermore, around the HEL location the LHC optics is constant throughout the fill cycle, allowing for no adjustment of the electron beam size at top energy. The angular kick θ experienced by a hadron particle at radius r traversing a hollow electron beam enclosing current I_{er} over the interaction length L can be expressed as:

$$\theta = \frac{1}{4\pi\epsilon_0}\frac{2I_{\mathrm{er}}L(1 \pm \beta_{\mathrm{e}}\beta_{\mathrm{h}})}{r\beta_{\mathrm{e}}\beta_{\mathrm{h}}c^2(B\rho)_{\mathrm{h}}},$$

where $v_{\mathrm{e}} = \beta_{\mathrm{e}}c$ is the electron velocity, $v_{\mathrm{h}} = \beta_{\mathrm{h}}c$ the hadron velocity, and $(B\rho)_{\mathrm{h}}$ is the magnetic rigidity of the LHC beam. For counter-propagating electron and hadron beams, the sign + applies ($v_{\mathrm{e}}v_{\mathrm{h}} < 1$), i.e. the kick is maximised. At Tevatron, during dedicated tests [5], kick amplitudes of the order of a fraction of micro-radiant were achieved. At HL-LHC it was estimated that similar values would provide the required depletion rate [1]. Given that at HL-LHC $\beta_{\mathrm{h}} \approx 1$ and the rigidity of the LHC beam at 7 TeV is about 23000 Tm, and knowing that typical values of the extraction energy for few Amperes electron beams are ~ 10 keV ($\beta_{\mathrm{e}} \approx 0.195$), the total current for the electron was specified to 5 A and the length of interaction of 3 m. This results in a kick $\theta = 0.3$ µrad for $r = 2$ mm, and hadron particles at $\sim 6.5\ \sigma_h$.

2.1 Hollow Electron Beam main parameters

At the HEL, the 5 A electron beam is generated by thermionic effect at an annular Scandium doped dispenser [12] (called hereafter cathode), heated to about $900°C$. The electrons are then extracted by applying a difference of potential (extraction voltage) between the cathode and a suitably shaped electrode (called anode) of 10 kV, which corresponds to the voltage necessary to extract 5 A with the given gun perveance [12]. The beam is magnetised (i.e. confined with solenoid fields) to counteract divergence due to space-charge forces, and guided from the gun to the collector, where it is dumped. The trajectory of the beam is bent at the injection into the LHC beam vacuum and extraction. Figure 1 shows the distribution of the magnetic field along the beam line providing the

2021 JINST 16 P03043

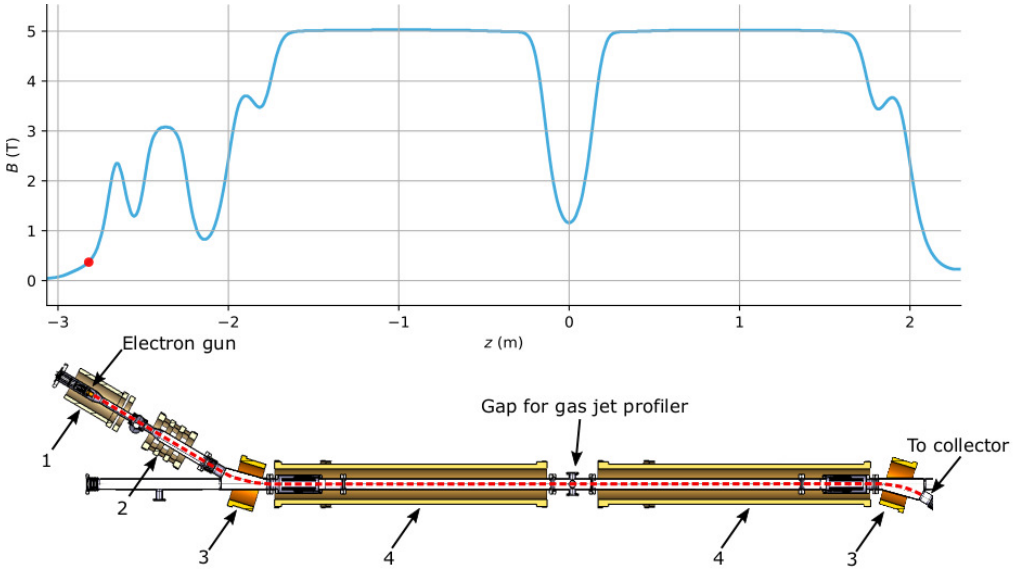

Figure 1. Guiding magnetic field profile along the red dashed line. The red dot on the magnetic field profile corresponds to the cathode position. Solenoids: 1 — gun solenoid (around the cathode) (0.37 T), 2 — "after valve" solenoid (3 T), 3 — bending solenoids (3.5 T), 4 — main solenoids (5 T).

necessary compression factor for operations at LHC beam energy equals to 7 TeV. The two main solenoids envelope the region where the electron and the proton beams overlap. The adjustment of the electron beam size is foreseen to be done by regulating the magnetic field at the gun (solenoid 1 in figure 1), which can vary between $\sim$ 0.3 T to 4 T, while keeping all other solenoid at constant current.

To correctly maintain alignment of the two beams, instrumentation is being developed that can continually operate under nominal machine conditions. Dedicated Beam Position Monitors, which will be installed at the entrance of the first main solenoid, and at the exit of the second, able to measure the relative position of the centre of mass of the two beams, with the required accuracy (in the range of a tenth of a mm), are under study. An other instrument under development is based on a laminar, supersonic gas curtain traversing the beams and producing light by beam-induced fluorescence of the gas molecules; the photons are not affected by the strong magnetic fields and the beams profiles are imaged by using an intensified camera. This produces a direct image of the two beams, similar to a standard screen measurement (Beam Gas Curtain, BGC monitor [13, 14]). The gap between the two main solenoids, shown in figure 1, was created to make room for the BGC monitor, where there is no deformation of the electron beam due to bending, and to reduce the stored energy of the main solenoids. The effect of the reduced magnetic field in the gap will be to have an enlarged electron beam, as detailed in the following. Figure 2 pictures the cross section of the electron and hadron beams overlapping inside the main solenoid, and the corresponding electric field seen by the hadron beams.

The minimum cathode size that could be produced, able to deliver such a current, has an internal diameter equal to 8.05 mm and external diameter 16.10 mm [12]. The electron beam, therefore, has to be compressed by a factor of 3.65 to comply with the required size for collimation, as in table 1, where r_1 and r_2 denote beam inner and outer radii, respectively. The size of the electron

2021 JINST 16 P03043

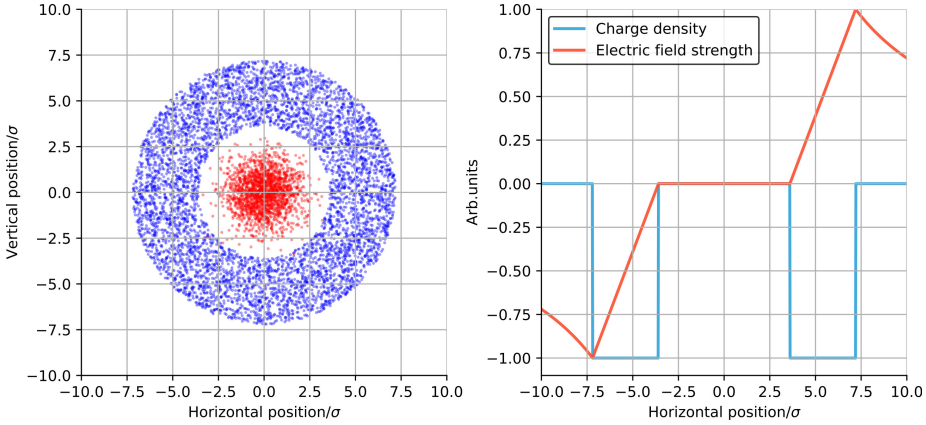

Figure 2. Cross section of the hollow electron beam and the hadron beam inside the main solenoid, for operations at LHC beam energy of 7 T (left), an electric field intensity for a uniformly distributed electron beam.

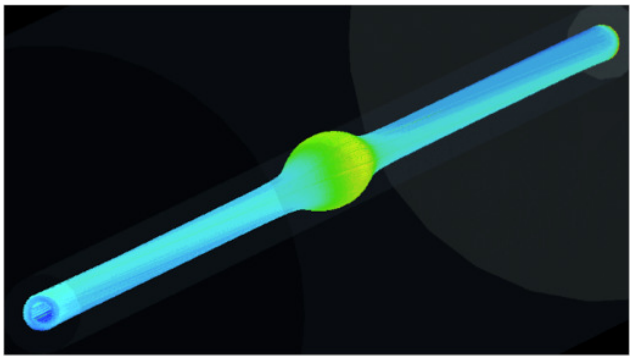

Figure 3. Example of the 3D beam shape along the main solenoids. The beam size increases at the gap where the magnetic field decreases.

beam in the region of interaction with hadrons can be controlled by adjusting the magnetic fields at the cathode, B_{cathode}, and at the main solenoids, B, in accordance with the expression:

$$\left(\frac{r_{1,2}}{r_{c_{1,2}}}\right)^2 = \frac{B_{\text{cathode}}}{B} \tag{2.1}$$

where $r_{c_{1,2}}$ refers to the cathode inner and outer radii, respectively. As explained before, for easiness of operation of the HEL, only the field at the cathode will be controlled, leaving all other magnets at constant current (or field). The drawback of this choice is that in the present configuration, optimised for operation at nominal LHC beam energy (7 TeV), is not suited to work at LHC beam at injection energy (450 GeV). In fact, given a maximum magnetic field at the mains of 5 T, a maximum field at the cathode of 4 T, and cathode raddi equal to 4.02–8.05 mm, the largest electron beam size achievable in the interaction region will be of $\simeq$ 3.6–7.2 mm, which is smaller than the LHC beam at injection energy (450 GeV). Operation of the HEL are discussed in more details in [1]. In the gap between the two main solenoids, the magnetic field inevitably decreases, with

2021 JINST 16 P03043

a minimum of $\sim$ 1.1 T at the gap centre. Here, as it can be estimated from equation (2.1), the corresponding electron beam radii will be $\simeq$ 2.35 $-$ 4.7 mm (for LHC at nominal energy). The expected beam shape evolution through the gap is shown in figure 3.

Table 1. Summary of the Hollow Electron Beam parameters

	Symbol	Value	Units
Electron current	I_{er}	5	A
Interaction length	L	3	m
Electron beam radius at 7 TeV LHC beam at main solenoid	$r_{1,2}$	1.1, 2.2	mm
Magnetic field in the interaction length (main solenoids)	B	5	T
Magnetic field at the gun	B	0.3 to 4	T
Vacuum chamber radius in the interaction length	R	60	mm

3 Electron beam dynamics and instabilities

As mentioned before, smooth operation of the HEL requires an electron beam generating an axially symmetric electromagnetic field affecting only halo particles, with zero field in the centre. This translates in the requirement of a perfectly annular electron beam, with uniform angular distribution. In this section, we give an overview of the physics linked to electron beam transport into a magnetic field structure and show analytically that the parameters chosen for the HL-LHC HEL shall guarantee a stable beam throughout the structure. In the following sections, these considerations will be corroborated by particle tracking simulations.

3.1 Pierce instability

The theoretical condition for the space charge limiting current, assuming one-dimensional electron motion, in a vacuum drift tube of radius R is given by [15, 16],

$$I_{\mathrm{e}} = \frac{2\pi\epsilon_0}{\left(\ln\frac{R}{r}\right)} U_{\mathrm{b}}^{\frac{3}{2}} \sqrt{\frac{8e}{27m_{\mathrm{e}}}} \tag{3.1}$$

where U_{b} is the beam potential at injection in the drift chamber, e is the electron charge, m_{e} the electron mass, r is the electron column radius. For $I > I_{\mathrm{e}}$, the electrons will be reflected backwards. Figure 4 shows the dependence of the critical current on the beam potential, R = 30 mm and r = 2.17 mm,[1] as at the HEL. Here one can see that if one would leave the electron potential at the extraction potential (10 kV, in section 2.1) as initially proposed [2, 17], it would be impossible to propagate 5 A current through the HEL structure.

Moreover, as the beam enters the vacuum chamber just after the gun, its potential will decrease to U_{b}, which can be estimated as approximately:

$$U_{\mathrm{b}} \approx U_0 + \frac{I}{2\pi\epsilon_0 v} \ln\frac{r_2}{a} \tag{3.2}$$

[1]This value actually corresponds to an electron beam of 3.55–7.1 σ_h, which is the value used at the time of the study. The conclusions presented in this paper are not affected by this small variation with respect to the present design requirements.

2021 JINST 16 P03043

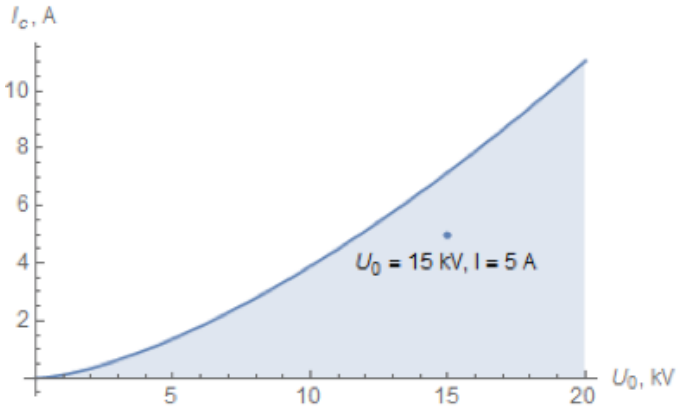

Figure 4. Critical current as a function of the beam potential at injection in the drift chamber, for a chamber of radius $R = 30$ mm and electron beam radius $r = 2.17$ mm. The blue dot denotes the accelerating potential chosen for the HEL.

where v is the average beam velocity at the entrance of a chamber of radius a and U_0 is the accelerating voltage (in our case the potential difference between the cathode and the grounded vacuum chamber). For $a = R = 30$ mm, $U_b - U_0 \approx 3$ kV. In order to transport full electron beam current through the HEL structure, and maintain a certain margin from the virtual cathode (or Pierce instability), it was chosen to set $U_0 = 15$ kV. This can be achieved by biasing the cathode at -15 kV (acceleration voltage), and the anode at -5 kV, in order to leave the extraction voltage (10 kV) invariant.

3.2 Diocotron instability

3.2.1 Beam rotation

The hollow electron beam generates a self-electric field, in the plane perpendicular to the longitudinal solenoid field B, applied to confine and guide the electrons. The self-electric field increases with increasing beam radius. For a hollow beam of inner radius r_1 and outer radius r_2, current intensity I, and longitudinal velocity v, it can be calculated from Poisson's law as:

$$E_r(r) = \begin{cases} 0 & \text{if } r < r_1, \\ \frac{I(r^2 - r_1^2)}{2\pi\epsilon_0 v (r_2^2 - r_1^2)} & \text{if } r_1 < r < r_2, \\ \frac{I}{2\pi\epsilon_0 v r} & \text{if } r_1 < r < r_2. \end{cases} \tag{3.3}$$

being $n_e = I/ev\pi(r_2^2 - r_1^2)$ the electron volume density. The electrons will therefore rotate at rotational (or angular) velocity [15, 18] expressed as

$$\vec{\omega_r} = \frac{[\vec{E} \times \vec{B}]}{B^2 r} \tag{3.4}$$

Due to the radial dependence of the rotational velocity, different layers of the electron beams will "slip" on each other. As it can be derived from equation 3.4, the higher the electron density, the higher the electric field and the larger the rotational velocity and its derivative with the radius, and vice

2021 JINST 16 P03043

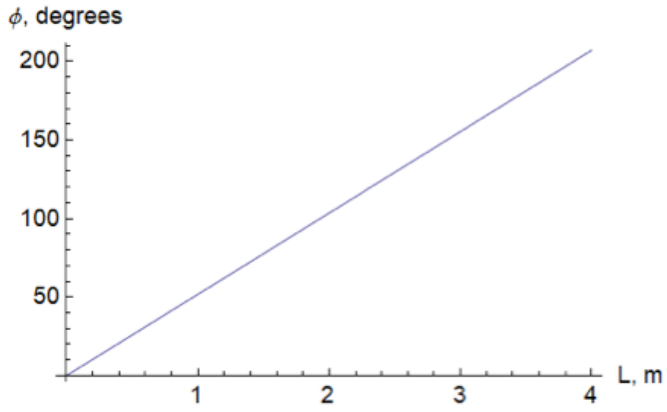

Figure 5. Maximum beam rotation for a 5 A electron beam with the outermost layer at 12 keV, progressing into a constant magnetic field of 5 T.

versa, the higher the magnetic field, the smaller the velocity and the smaller its derivative. Without going into detailed considerations, one can qualitatively say that the magnetic field rigidifies the beam and help to preserve its shape and distribution, since it avoids the development of turbulence's, as shown in the following section. One way to evaluate how prone the beam is to instabilities, is to estimate the maximum angle of rotation of the whole beam moving from the beginning to the end of the main solenoid as

$$\Phi_{\max} \approx \omega_{r_2} \frac{L}{v} \tag{3.5}$$

corresponding to the angular velocity of the outer most layer of the beam, where v is the longitudinal beam velocity, and L/v is the time for the beam to travel from one end to the other of the interaction region. The dependence of the rotation angle on the length of the main solenoid is presented in figure 5 for a velocity $v_{r_2} = 0.62 \times 10^8$ m/s (corresponding to an electron beam energy $\sim$ 12 keV (that is assuming $U_{\mathrm{b}} \sim 12$ kV as derived from the previous section, which translates to a kinetic energy $E_{\mathrm{k}} \sim 12$ keV), beam current $I = 5$ A, and field at the main solenoid $B = 5$ T.

In the case of the HEL, the rotation of the beam from the beginning of the first main solenoid to the end of the second one is expected to be around 180°, as confirmed by numerical simulation (section 4). Smaller electron beam sizes would entail larger electric field and rotational speed, and make the beam more prone to instability. It should be noted that along a curved trajectory, like at the injection of the electron beam into the LHC vacuum chamber, there are additional transverse forces linked to the bending, deriving from the magnetic field gradient and from the centrifugal force, which will affect the processing of the electrons. We define $\omega_{\mathrm{ce}} = \mathrm{e}B/m_{\mathrm{e}}$ the electron cyclotron rotation frequency, $v_\perp = r_{\mathcal{L}}\omega_{\mathrm{ce}}$, $r_{\mathcal{L}}$ being the Larmor radius, $v_\parallel$ the longitudinal velocity, parallel to the magnetic field lines, and ρ the trajectory bending radius. The guiding centre of the particles' azimuthal trajectory follows the relation

$$\frac{dr_{\text{guiding centre}}}{dt} = v_\parallel \frac{\vec{B}}{|B|} + \frac{[\vec{E} \times \vec{B}]}{B^2} + \frac{1}{2} v_\perp^2 r_{\mathcal{L}} \frac{[\vec{B} \times \nabla \vec{B}]}{B^2} - \frac{v_\parallel^2}{\omega_{\mathrm{ce}} B} \frac{[\vec{\rho} \times \vec{B}]}{\rho^2}$$

It is easy to verify that both contributions from the magnetic field gradient and the trajectory bending are negligible with respect to the $\vec{E} \times \vec{B}$ contribution.

2021 JINST 16 P03043

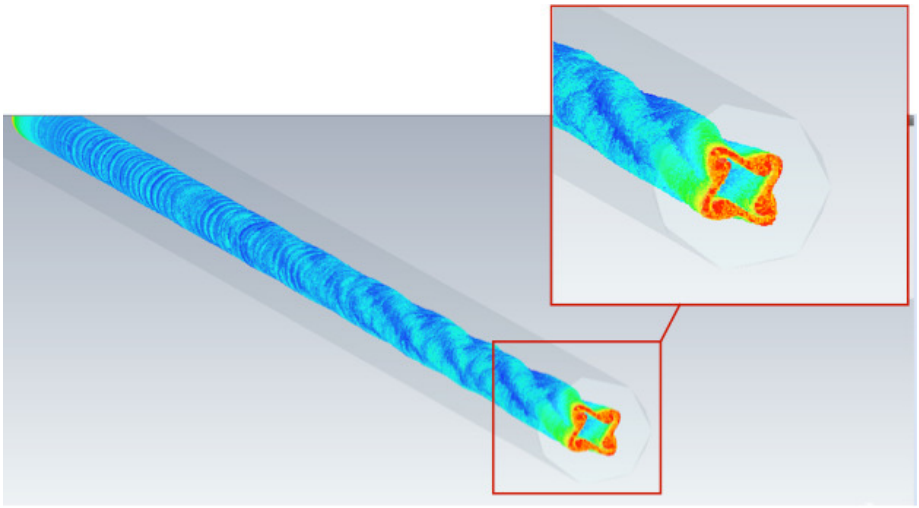

Figure 6. Illustrative example of a simulation of beam fragmentation into clusters due to diocotron instability.

3.2.2 Stability criterion

Diocotron instability (also called "slipping-stream" instability) is driven by a sufficiently strong shear in the angular rotation of the beam. Wherever the beam density profile has azimuthal perturbations, the shear in the angular flow velocity can provide enough energy to drive instabilities, i.e. growth of distribution perturbation up to beam disruption. Figure 6, visualises an example of a hollow electron beam that is annular at the beginning of its motion and that, after some time, starts to deform and cluster into islands (4 in the example).

In this section, we will show analytically that an electron beam with parameters like at the HEL, will not grow unstable, since the characteristic time for instabilities to develop is much longer than the time for the beam to travel from the source (electron gun) to the dump (collector). We assume we have uniform current distribution and that we can use the approximation of low-density plasma [18], defined as

$$\frac{\omega_{\mathrm{pe}}^2}{\omega_{\mathrm{ce}}^2} = \frac{n_{\mathrm{e}} m_{\mathrm{e}}}{\epsilon_0 B^2} = \frac{I m_{\mathrm{e}}}{\pi \epsilon_0 v (r_2^2 - r_1^2) B^2} \approx 1.810^{-4} \ll 1 \tag{3.6}$$

where $\omega_{\mathrm{pe}} = \sqrt{n_{\mathrm{e}} \mathrm{e}^2 / \epsilon_0 m_{\mathrm{e}}}$ is the plasma frequency (frequency at which charge particles oscillate into a plasma, following a perturbation from uniform density distribution), $n_{\mathrm{e}} = I/ev\pi(r_2^2 - r_1^2)$ the electron volume density, already defined in the previous section, and $\omega_{\mathrm{ce}} = \mathrm{e}B/m_{\mathrm{e}}$ the cyclotron rotation frequency mentioned in the previous section.

The stability criterion for our beam is given by the inequality [18–20]:

$$\left[-l\left[1 - \left(\frac{r_1}{r_2}\right)^2\right] + 2 - \left[\left(\frac{r_1}{R}\right)^{2l} + \left(\frac{r_2}{R}\right)^{2l}\right]\right]^2 \geq 4\left(\frac{r_1}{r_2}\right)^{2l}\left[1 - \left(\frac{r_2}{R}\right)\right]^2 \tag{3.7}$$

with R the radius of the vacuum chamber, as mentioned before, and $l = 1, 2, 3, \ldots$ the azimuthal mode number of the perturbation. Note that this stability criterion depends on geometrical parameters

2021 JINST 16 P03043

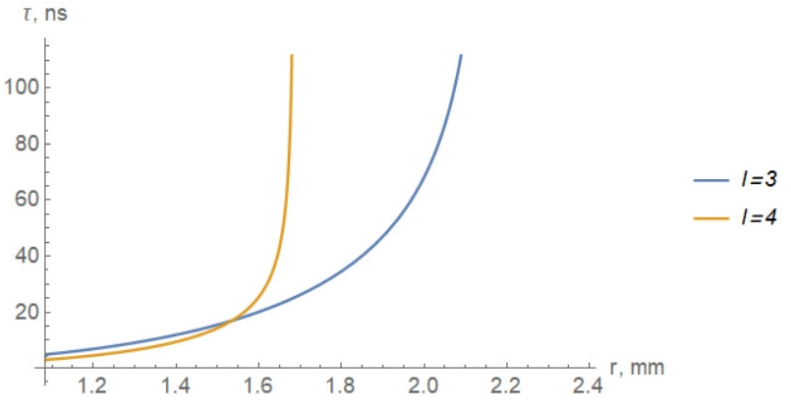

Figure 7. Dependence of the instability growth rate on the beam outer radius, at fixed inner radius $2r_1 = 2.17$ mm, for the diocotron instability mode $l = 3$ (blue line) and $l = 4$ (yellow line).

only, i.e. on the beam radii and the radius of the vacuum chamber. The beam current and external magnetic field will, on the other hand, influence the instability characteristic time of growth τ, as:

$$\tau^{-1} = \frac{1}{2}\omega_{\mathrm{D}}\sqrt{4c_l - b_l^2} \tag{3.8}$$

where $\omega_{\mathrm{D}} = \omega_{\mathrm{pe}}^2/2\omega_{\mathrm{ce}}^2 = en_{\mathrm{e}}/2\epsilon_0 B$ is an "effective diocrotron frequency", and

$$b_l = -l\left[1 - \left(\frac{r_1}{r_2}\right)^2\right] + \left[\left(\frac{r_1}{R}\right)^{2l} + \left(\frac{r_2}{R}\right)^{2l}\right]$$
$$c_l = -l\left[1 - \left(\frac{r_1}{r_2}\right)^2\right]\left[1 - \left(\frac{r_1}{R}\right)^{2l}\right] - \left[1 - \left(\frac{r_1}{R}\right)^{2l}\right]\left[1 - \left(\frac{r_2}{R}\right)^{2l}\right]$$

As it can be derived from the stability criterion 3.7, beams with radii having ratio $r_2/r_1 > 2$ are stable. If the ratio is exactly $r_2/r_1 = 2$, one can still call the beam "stable", since τ is larger than the time for the electron beam to cross the main solenoids (estimated to be ~ 57 ns). To show that, let us consider the case where $r_2/r_1 = 2 - \delta \simeq 2$, that is a deviation from the designed parameters $\delta \ll 1$. Fixing the inner diameter $2r_1 = 2.17$ mm, we look at the dependency of τ on the value of the beam outer radius r_2. To this end, let's consider the inequality 3.7 relative to r_2 for the different mode numbers l. The mode with $l = 1$ is always stable. The $l = 2$ mode is much slower (100 time) than the $l = 3$ mode, so we look here in more details at the latter: the dependence of $\tau(l = 3)$ with outer beam radius, pictured in figure 7 with a blue line, shows for $r_2 = 2.17$ mm, i.e. $r_2/r_1 = 2$, an asymptote. Let's assume now a beam with $r_2 \approx 2.39$ mm, i.e. 10% larger than the design value of 2.17 mm. In this case $\tau \approx 75$ ns, which is larger than the time for the beam to travel through the main solenoid, implying that there is not enough time for the instability to develop.

Higher l modes are less dangerous for two reasons: first, for these modes τ is larger than for the $l = 3$ mode; second, if we take the example of $l = 4$, the vertical asymptote position is significantly shifted to the left (figure 7, yellow line), which means that only larger deviations from the designed parameters will lead to this diocotron instability mode.

2021 JINST 16 P03043

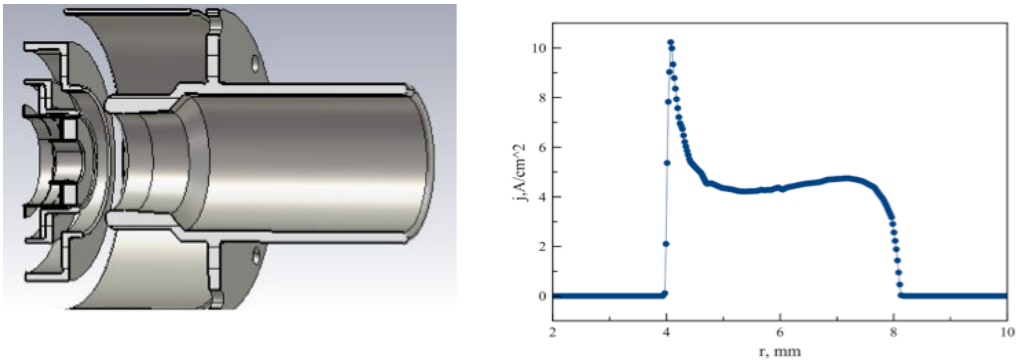

Figure 8. Electron gun mechanical layout as used in CST PS simulations (left), and estimated electron beam current density at 60 mm from the cathode surface (right).

4 Simulations for the HEL electron beam and feedback to the HEL design

Electron beam dynamics was simulated with CST (Computer Simulation Technology) Particle Studio (PS) for the analysis of charged particle dynamics in 3D electromagnetic fields. The detailed scope of the investigation was to check that the HEL design parameters would guarantee a stable electron beam, with negligible deformation from the gun cathode (annular) shape down to the exit of the hadron-electron interaction region. Two solvers were compared: Particle-Tracking (TRK) Solver for particles in static fields including space charge, and Particle-In-Cell (PIC) Solver for self-consistent transient field and particle solver including full space charge effects at all frequencies. Both solvers turned out to be computationally very heavy, given the size of the beam (few millimetres, requiring a mesh size in the sub-millimetre) and the size HEL structure (about 5 metres in total). For the scope of the study, the two solvers seemed equivalent (did not show different results for scaled down problems), but the PIC solver could not be used for a large structure, since the program would crash. That is the reason why in this paper we present only the results obtained with the TRK solver. To simulate the electron beam dynamics with a sufficiently high accuracy, we divide the beam line into three segments: (1) from the electron gun up to the injection into the interaction region; (2) from the injection the through the end of main solenoids; (3) from the end of the main solenoids to the collector. Each segment represents an independent simulation setup; the electron distribution at the beginning of segment (1) is estimated from the gun simulation, and the output distribution of segment (1) and (2) are used to start the simulations of segment (2) and (3) respectively.

4.1 Hollow beam generation at the electron gun

As mentioned before, the 5 A electron beam is generated at the electron gun (using an annular cathode of radii 4.02–8.05 mm, and 10 kV extraction voltage) and accelerated to 15 kV by applying a negative voltage of −15 kV at the cathode and having the vacuum chamber grounded.

The profile electron density emission was simulated with CST PS for a geometry as shown in figure 8. These results were compared [21] against others produced with WARP [22] and with UltraSAM [23]. The results looked very similar, with CST producing the highest central peak (9 A/cm^2 with CST, against 6.26 A/cm^2 with UltraSAM and 7 A/cm^2 with WARP), while all gave about 4 A/cm^2 for radii > 5 mm. All gun simulations also compared very well (about a factor

2021 JINST 16 P03043

of 2 in absolute value, but very similar shapes) with the measurements of beam profile performed at Fermilab [5]. The peaked profile of the electron beam distribution, which is a desired feature allowing a larger electric field at the innermost layers of the hollow beam, and therefore an enhanced kick to the hadron beam particles at smaller amplitude, is achieved by the electrodes placed around the cathode.

4.2 Hollow beam in the entrance of the interaction region

Transport simulations of intense beams that are subject to instabilities leading to distortion of the beam profile, require the optimization of the computational mesh to minimize errors in calculating of self-fields. The TRK solver uses hexahedral meshing. The accuracy depends on the mesh size, the number of the macro-particles and the tilt between the equipotential lines of the fields and the mesh lines. If the grid is parallel to equipotential lines, the distance between the mesh nodes and the external boundaries is constant throughout the simulation path. This is the case in the beam simulation in the main solenoids (segment (2)), but not so in the injection arm. Here, the variation of the distance between the mesh nodes and boundaries through segment (1) has, as a result, different accuracy in the estimation of the beam potential for the different mesh nodes. Of course, decreasing the mesh size would improve the accuracy. Unfortunately, CST does not allow different mesh sizes for the beam differently and the rest of the structure so the number of meshes explodes as the mesh size is reduced. The limit we found is a mesh size of $0.5 \times 0.5 \times 0.5\,\mathrm{mm}^3$. Figure 9 shows, as an example, a cross section of the HEL electron beam at the beginning of the main solenoid (after simulation of beam transport though segment (1)). The colour coding refers to the kinetic energy of the macro-particles. The solenoid field at the gun is 0.37 T and 5 T at the main solenoid, with a profile shown in figure 2. The results correspond to mesh sizes of $0.5 \times 0.5 \times 0.5\,\mathrm{mm}^3$ (left hand side) and $1 \times 1 \times 1\,\mathrm{mm}^3$ (right hand side). One can see that the beam shape looks similar in the two cases, but the kinetic energy distribution of the beam is different. We are aware that the limitation in mesh size, plus the fact that we inevitably need to use macro-particles, introduces numerical errors. The comparison with the theoretical treatment of the problem makes us confident that these errors should not invalidate the conclusion of the study. For these simulations, the solenoid field at the gun is 0.37 T and 5 T at the main solenoid, with a profile shown in figure 1. The beam is progressively compressed the inner radius to 1.08 mm and the external to 2.17 mm as the magnetic field is increased. The change in particles kinetic energy amplitude and distribution is a result of the potential sagging — as from equation (3.2), and the asymmetry of the vacuum chamber at the intersection between the injection arm and the main solenoids (figure 10). The non-uniform distance between the electron beam and the chamber walls leads to an imbalance of the electrical forces applied to the beam. Since the beam shape is frozen by the magnetic field, the overall forces are compensated by an increase in the electrons potential energy and a reduction of their kinetic energy in some portion of the beam as shown in the figure 9. Taking into account the beam and vacuum chamber parameters, and the expression 3.2, we can theoretically estimate the difference between the potentials of the particles to be about 1.3 kV, which is in good agreement with the difference estimated with $0.5 \times 0.5 \times 0.5\,\mathrm{mm}^3$ mesh size (1.2 kV).

2021 JINST 16 P03043

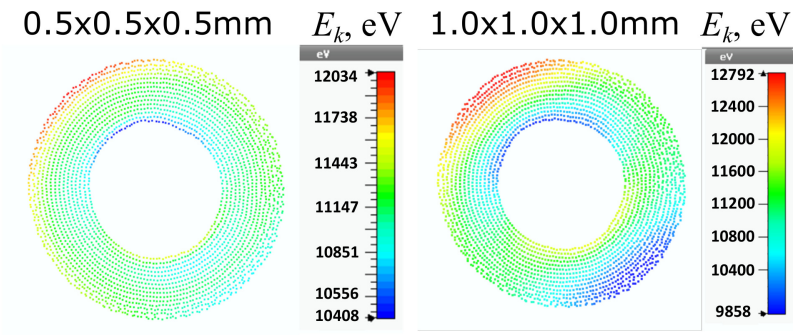

Figure 9. Comparison simulation results at the end of the injection line (segment (1)) for different mesh sizes.

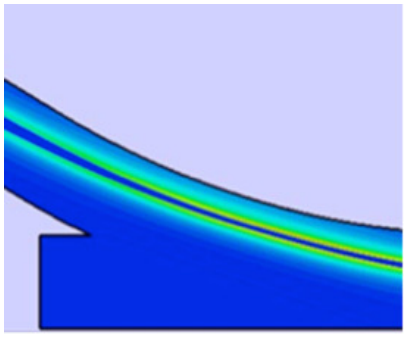

Figure 10. Electron beam trajectory at the injection into the LHC vacuum beam chamber, as resulting from simulations.

4.3 Hollow beam at the end of the interaction region

Figure 11 shows beam dynamics simulation results at the beginning and at the end of the main solenoids, for a $0.5 \times 0.5 \times 0.5\,\mathrm{mm}^3$ mesh size. Several features can be observed: the asymmetric distribution of kinetic energy is preserved along the interaction region, but not increased since the beam travels along the axis of a cylindrical chamber. The rotation of the beam (as can be inferred by looking, for example, at the position of the portion at higher kinetic energy — in red in the picture) is about 180°, as predicted in section 3.2.1, for a length corresponding to the main magnets plus the gap in between (total length $\sim 3.3\,\mathrm{m}$). The inner layers of the beam are slightly distorted at the exit of the second main solenoid. The reason for this distortion, as mentioned in a previous section, is due to the redistribution of the charge density and distortion of the beam shape deriving from layers slipping on each other. This distortion breaks the azimuthal beam symmetry and results in a residual electric field inside the hollow of about 10 kV/m.

Figure 12 shows a two-dimensional map of the electric field in a $5 \times 5\,\mathrm{mm}$ cross section at the end of the interaction region and the field distribution along one of the transverse coordinates across the beam. The energy profile as calculated analytically with formula 3.5 is added to the right graph. The difference between the analytical expression and the CST calculation for the maximum amplitude is less than 4%. The value of the scattered field amplitude inside the hollow beam does not exceed 10 kV/m.

2021 JINST 16 P03043

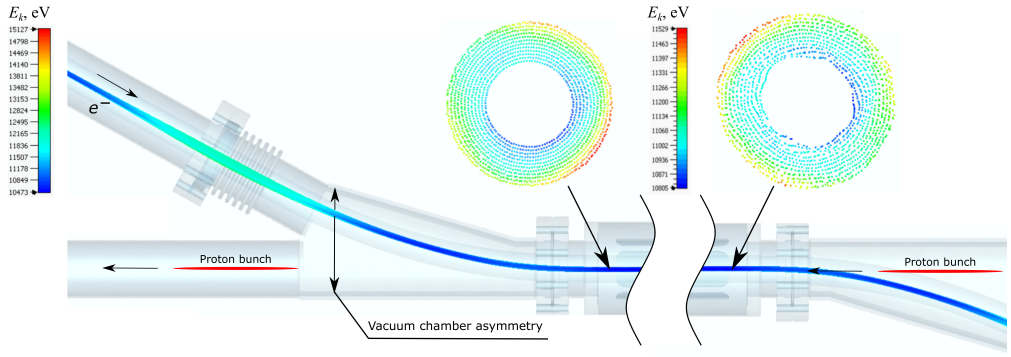

Figure 11. Results of hollow electron beam transport simulations. The maximum beam shape distortion is observed at the end of the main solenoid.

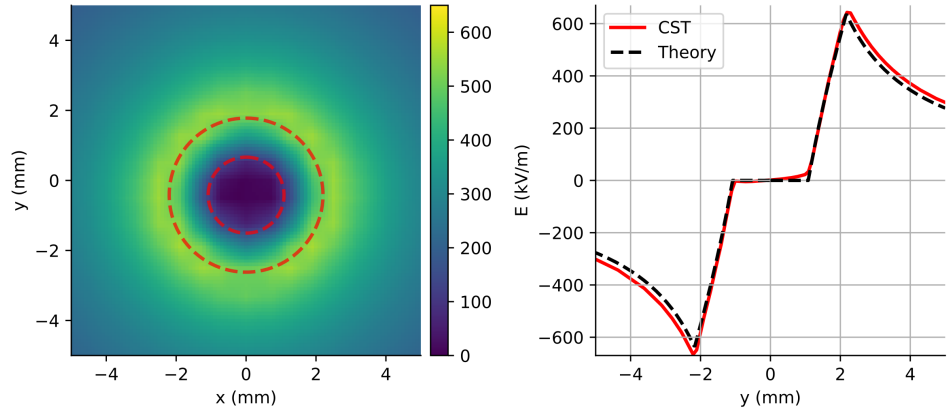

Figure 12. Right: 2-D electric field map of hollow beam at the end of interaction region (the red dashed line shows the beam boundaries); left: comparison of the calculated and analytical electric field distribution in the plane perpendicular to the beam axes.

5 Conclusions and future outlook

In this paper we presented an overview of the studies undertaken to support the design of the HL-LHC hollow electron lens. We proved that with the parameters of the HL-LHC system, the high intensity electron beam can be transported without reflection if the accelerating voltage is set to 15 kV, and showed that with 5 T field in the main solenoids the beam remains stable, and does not undergo to significant deformation. Simulation results were corroborated by analytical computations, while experimental benchmarking could only be carried out for the simulations of the electron gun emission. Further studies will include measurements of a prototype of the HEL electron gun at the CERN Electron Beam Test Stand, where, even if with little or no compression due to the limited magnetic field (around 0.4 to 0.5 T), conditions of beam instability can be created. A more in depth analysis of the mesh size effect should be carried out to better understand its effect on the electron beam distribution and integrated field seen by the LHC beam. Future studies will also look at how to operate the correctors in order to obtain a smooth injection, and to verify that the electrons are efficiently dumped into the collector.

2021 JINST 16 P03043

Acknowledgments

This work is supported by the HL-LHC project. The authors would like to warmly thank Giulio Stancari for sharing his wide knowledge on the subject. Sergey Sadovich for his critical view and stimulating contribution on the simulations. Diego Perini and Antti Kolehmainen for the mechanical design and for being opened to our input and changes. Stefano Redaelli for his support throughout the studies, and useful discussions.

References

[1] S. Redaelli, R. Bruce, O. Brüning, A. Kolehmainen, G. Ferlin, A. Foussat et al., *Hollow electron lenses for beam collimation at the High-Luminosity Large Hadron Collider (HL-LHC)*, in *ICFA Beam Dynamics Newsletter #81* (2021).

[2] G. Stancari, V. Previtali, A. Valishev, R. Bruce, S. Redaelli, A. Rossi et al., *Conceptual design of hollow electron lenses for beam halo control in the Large Hadron Collider*, Tech. Rep., CERN-ACC-2014-0248, FERMILAB-TM-2572-APC, CERN, Geneva (2014).

[3] M. Fitterer, G. Stancari, A. Valishev, S. Redaelli and D. Valuch, *Resonant and random excitations on the proton beam in the Large Hadron Collider for active halo control with pulsed hollow electron lenses*, *Phys. Rev. Accel. Beams* **24** (2021) 021001 [arXiv:1804.07418].

[4] D. Mirarchi and et al., *Non-linear dynamics of proton beams with hollow electron lens in the CERN High-Luminosity LHC*, submitted to the *Eur. Phys. J. Plus* (2021).

[5] G. Stancari, A. Valishev, G. Annala, G. Kuznetsov, V. Shiltsev, D.A. Still et al., *Collimation with hollow electron beams*, *Phys. Rev. Lett.* **107** (2011) 084802 [arXiv:1105.3256].

[6] G. Stancari, *New Methods of Particle Collimation in Colliders*, in *Meeting of the APS Division of Particles and Fields*, 10, 2011 [arXiv:1110.0144].

[7] G. Stancari et al., *Collimation studies with hollow electron beams*, in proceedings of the *International Particle Accelerator Conference*, San Sebastián, Spain, 4–9 September 2011, pp. 1939–1941.

[8] G. Stancari et al., *Beam experience at the tevatron and status of the hollow electron-lens hardware*, https://indico.cern.ch/event/213752.

[9] I. Béjar Alonso, O. Brüning, P. Fessia, L. Rossi, L. Tavian and M. Zerlauth, *High-Luminosity Large Hadron Collider (HL-LHC): Technical design report*, CERN Yellow Reports: Monographs, CERN, Geneva, 2020, DOI: 10.23731/CYRM-2020-0010.

[10] M. Gonzales de la Aleja and P. Fessia, *Preliminary integration of the hollow electron lens*, CERN EDMS Doc. No. 1764989 v. 3 (2017).

[11] R. De Maria, R. Bruce, D. Gamba, M. Giovannozzi and F. Plassard, *High Luminosity LHC optics and layout HLLHCV1.4*, *J. Phys. Conf. Ser.* **1350** (2019) 012001.

[12] D. Perini, A. Kolehmainen, G. Stancari and S. Sadovich, *Design of high-performance guns for the HL-LHC HEL*, in *ICFA Beam Dynamics Newsletter #81* (2021).

[13] R. Veness, M. Ady, N. Chritin, P. Forck, J. Glutting, O. R. Jones et al., *Development of a beam-gas curtain profile monitor for the high luminosity upgrade of the LHC*, in proceedings of the *international Beam Instrumentation Conference*, Shanghai, China, 9–13 September 2018, pp. 472–476.

2021 JINST 16 P03043

[14] H. Zhang, M. Ady, A. Alexandrova, E. Barrios Diaz, N. Chritin, P. Forck et al., *A supersonic gas jet-based beam profile monitor using fluorescence for HL-LHC*, in proceedings of the *International Particle Accelerator Conference* , Vancouver, Canada, 29 April–4 May 2018, pp. 1891–1894.

[15] M. Reiser, *The physics of charged-particle beams*, Addison-Wesley (1994).

[16] J. D. Lawson, *The physics of charged-particle beams*, Clarendon Press, Oxford (1977).

[17] S. Redaelli, *Functional specifications and parameter requirements*, presentation at the *International Review on the e-lens concept readiness for integration into the HL-LHC baseline*, CERN, Geneva, Switzerland 19–20 October 2017.

[18] R. Davidson, *An introduction to the physics of nonneutral plasma*, Frontiers in Physics, vol. 81, Addison-Wesley, Redwood City, CA, U.S.A. (1990).

[19] R.C. Davidson and G.M. Felice, *Influence of profile shape on the diocotron instability in a non-neutral plasma column*, *Phys. Plasmas* **5** (1998) 3497.

[20] T.C. Genoni and W.A. Proctor, *Upper bound for the space-charge limiting current of annular electron beams*, *J. Plasma Phys.* **23** (1980) 129.

[21] D. Nikiforov, A. Levichev, A. Barnyakov and M. Maltseva, *Results from electron beam simulations with latest design*, presented at the *HiLumi WP5/WP13 joint meeting on Hollow Electron Lens*, CERN, Geneva, Switzerland, 9 March 2018.

[22] D.P. Grote, *The WARP code: Modeling high intensity ion beams*, *AIP Conf. Proc. 749* (2005) 55.

[23] A. Ivanov and M. Tiunov, *UltraSAM - 2d code for simulation of electron guns with ultra high precision*, in proceedings of the *European Particle Conference*, Paris, France, 3–7 June 2002, pp. 1634–1636.

2021 JINST 16 P03043